Cartesian normal-mode models for a mid-size laboratory water tank

Kaylyn N. Terry, Cameron T. Vongsawad and Tracianne B. Neilsen

Citation: Proc. Mtgs. Acoust. **45**, 070007 (2021); doi: 10.1121/2.0001567
View online: https://doi.org/10.1121/2.0001567
View Table of Contents: https://asa.scitation.org/toc/pma/45/1
Published by the Acoustical Society of America

Volume 45 http://acousticalsociety.org/

181st Meeting of the Acoustical Society of America

Seattle, Washington

29 November - 3 December 2021

Underwater Acoustics: Paper 3aUW1

Cartesian normal-mode models for a mid-size laboratory water tank

Kaylyn N. Terry, Cameron T. Vongsawad and Tracianne B. Neilsen
Department of Physics and Astronomy, Brigham Young University, Provo, UT, 84602; kaylynterry@gmail.com; cvongsawad@gmail.com; tbn@byu.edu

A laboratory water tank at Brigham Young University is being characterized, and a suitable model is needed to describe the sound propagation, which includes realistic boundary conditions. Two Cartesian normal-mode models are compared: one begins with pressure release boundary conditions then adds wall losses and the other begins with rigid boundary conditions for the walls and incorporates finite impedance through spatially averaged absorption. The models are updated to remove assumptions for smaller glass tanks and to include estimates of the characteristic acoustic impedance of the wall material. Each model is sensitive to the number of modes used. The modeled transmission loss values at 10 Hz to 100 kHz are computed for the rectangular acrylic tank (3.6 m x 1.2 m wide with water depths of 0.47 m and 0.24 m x 0.48 m). The modeled values are compared to measured data via relative transmission loss estimates as a function of distance. The tank sound propagation model will allow us to model our tank, simulate the sound field for optimization problems, and create accurate training data for machine learning applications.

Published by the Acoustical Society of America

 https://doi.org/10.1121/2.0001567

1. INTRODUCTION

Models for sound propagation in a rectangular enclosure are often solutions to the 3-D wave equation in Cartesian coordinates based on normal modes, and the simplest solutions use pressure release or rigid boundary conditions. These models can be extended to realistic rectangular parallelpiped listening spaces if the finite impedance of the surfaces are accounted for. We are interested to see if these methods, which are common in room acoustics, can be used to model the sound propagation in a rectangular parrallelpiped water tank. The simplest approach would be to assume the water is surrounded by pressure release or rigid surfaces, but a more realistic approach would include finite impedance boundary conditions.

Two Cartesian normal mode models are evaluated in this paper. The first finite impedance model, found in the textbook by Pierce,[1] begins with rigid boundary conditions for the walls and incorporates finite impedance using the spatially averaged absorption. The second model is inspired by recent work by Novak *et al.*[2] They showed excellent agreement between measurements and a Cartesian normal mode model for low-frequency sound propagation in small glass water tanks with thin walls and finite impedance. This excellent agreement came after making several assumption, which do not apply to our larger, acrylic tank. By removing those assumptions and including realistic boundary conditions, we get a second finite impedance model to compare with the one from Pierce. While other studies have looked at propagation in tanks, including Refs. 3–5, this work studies the applicability of two finite-impedance Cartesian normal-mode models to underwater sound propagation in a open, laboratory water tank.

2. SETUP

The open-air rectangular laboratory water tank, shown in Fig. 1, was made by Engineering Laboratory Design Inc. (Lake City, Minnesota, USA) and is constructed of scratch resistant acrylic panels that are 2.54 cm thick. The tank is 3.66 m long by 1.22 m wide with a maximum water depth, h_w, of 0.91 m, corresponding to a maximum fill volume of 4077.6 liters. On the far side of the tank at the top of Fig. 1, are two UR10e robotic arms used for positioning the hydrophones in the tank. The hydrophones connect to a measurement chain as will be explained below. The left side of Fig. 1 shows the water filtration system that filters, sanitizes, controls the water temperature, and reduces bubbles in the tank. (See Ref. 6 for details.)

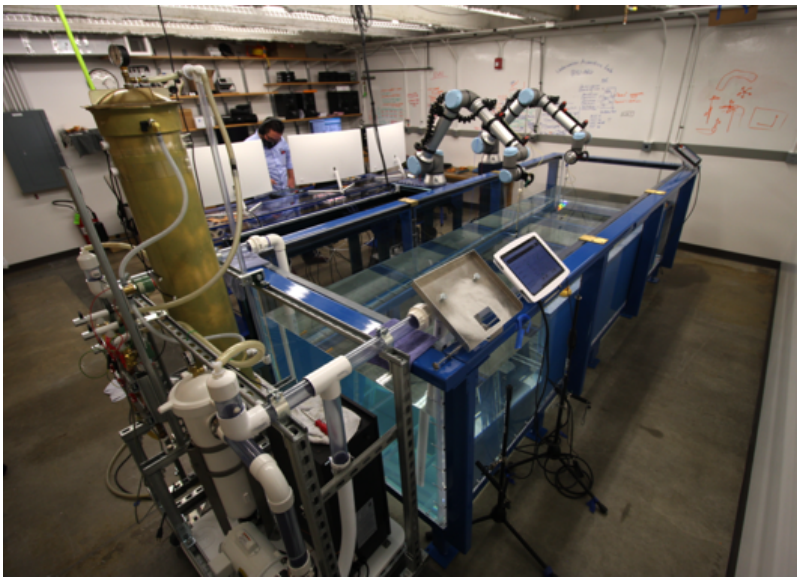

Figure 1: BYU's acrylic water tank and robotic positioning and filtration systems

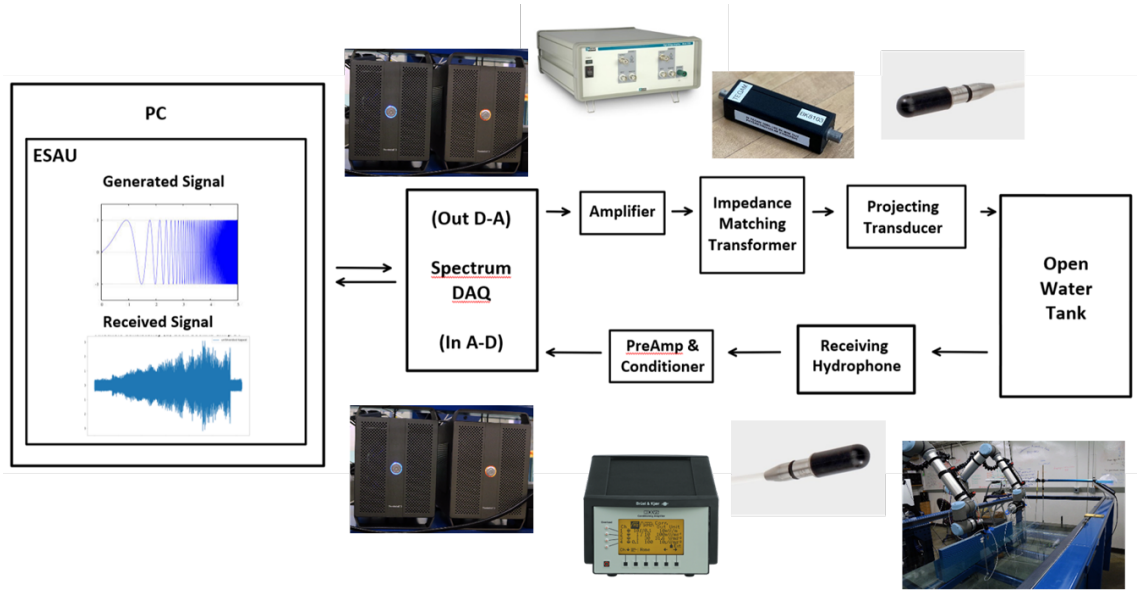

Figure 2: Data acquisition chain

A. DATA ACQUISITION CHAIN

An automated measurement system (shown in Fig. 2) was used with Bruel and Kjaer 8103 hydrophones to gather all the data analyzed in this paper. First, a swept sine signal is generated in our LabView interface. This signal is passed through a Spectrum output card (M2p.6546-x4), and then a power amplifier (TEGAM 2350), which provides a gain of 50. The output from TEGAM goes through an impedance matching transformer designed for any signal above 10 kHz. The signal then reaches the projecting transducer (a B&K 8103) and is transmitted through the water to the receiving hydrophone (another B&K 8103). The received signal travels to a B&K signal conditioner NEXUS and then to Spectrum input card (M2p.5932-x4). Now digitized, the received signal is displayed in the LabView program alongside the transmitted signal and saved. More details are available in Ref. 6.

B. THROUGH THE SENSOR CALIBRATION

The contribution of the measurement chain components to the frequency response can ideally be accounted for by using the individual calibrated responses of each component (shown in Fig. 2). Alternately, the cumulative contribution of all components may be accounted for by understanding the total through-the-sensor (TTS) response, $h_{\mathrm{TTS}}(t)$, is obtained from the calibration measurement. Using a closely spaced source and receiver pair, a recorded chirp is processed via cross correlation to obtain the impulse response of the system.[7–12] This procedure uses techniques in room acoustics and is similar to the procedure in Ref. 13, except that they were doing source characterization and we are obtaining the frequency response of the measurement chain with minimal propagation effects.[6] The TTS response is then used as a filter (in deconvolution) on subsequent measurements to remove $h_{\mathrm{TTS}}(t)$ and obtain the impulse response, $h(t)$, corresponding to sound propagation in the water tank. The directivity of the transducers over the bandwidth of interest is omnidirectional, except for a null in the direction of the cable, which is not in the direction of interest because the transducers are mounted horizontally.

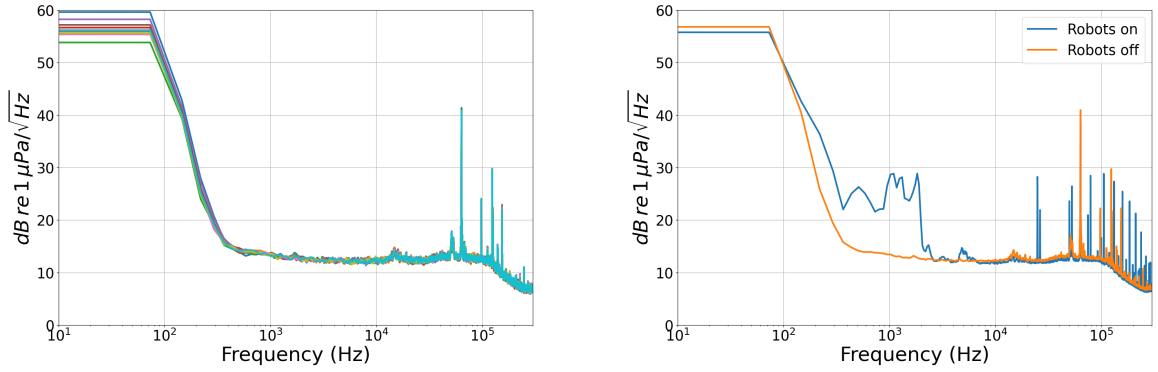

(a) *(b)*

Figure 3: (a) Spectral density levels for ten ambient noise measurements in the tank when the robots and positioning system are turned off. (b) Average spectral density levels (over ten ambient noise measurements) when the robots and positioning system are on (blue line) and when turned off (orange line).

C. AMBIENT NOISE

To investigate the ambient noise levels in our tank, several iterations of ten sequential ambient noise measurements were taken in the middle and at both ends of the tank. In each case, the ambient noise proved to be repeatable, as shown by examining the spectra of ten repeated ambient measurements in Fig. 3(a). This repeatability in ambient noise allows the above TTS calibration to effectively remove that noise from measurements. The received signal of each ambient measurement has an approximately Gaussian distribution, as seen in Fig. 4: Mean = -0.0030, Standard Deviation = 0.0050, Variance = 2.5e-5, Skewness = -0.041, Kurtosis = -0.35. The ambient noise does change, however, when the positioning robotic arms are turned on or off, as shown in Fig. 3(b). The ambient noise measurements taken when the robots were on were also repeatable, both with a noise floor around 12 dB above 2 kHz.

3. MODELS

In Cartesian coordinates (x, y, z), the time-independent 3D wave equation, otherwise known as the Helmholtz equation, can be expressed in terms of mode functions Ψ_m:

$$\nabla^2 \Psi_m(x_0, y_0, z_0) + k_m^2 \Psi_m(x, y, z) = 0, \tag{1}$$

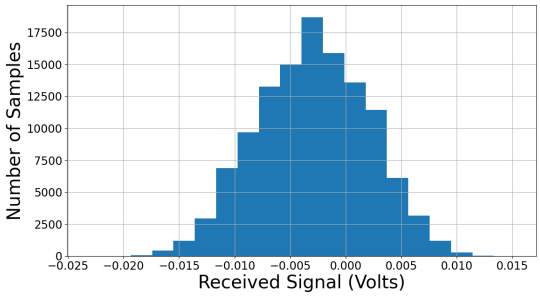

Figure 4: A histogram of the ambient measurements in Fig. 3a.

where m corresponds with the mode number. The modal eigenvalues are calculated by $k_m = \frac{2\pi f_m}{c}$, where f_m are the eigenfrequencies and c is the speed of sound in the water. Each of the calculations in the following sections is frequency dependent. The source position is denoted by (x_0, y_0, z_0) and the receiver position is (x, y, z). For this equation, the two ideal boundary conditions are (1) a pressure release boundary and (2) a rigid wall boundary. Our laboratory tank has one pressure release boundary at the water to air surface, but the five water to acrylic boundaries are not rigid walls or pressure release boundaries. An in-between condition is needed to more realistically represent our tank walls. In this paper, we explore two finite-impedance models to compare with measured data in our tank: "Model P" is explained in Pierce's book, *Acoustics*,[1] and "Model N" is influenced from a paper by Novak *et al.*[2]

A. MODEL P

Model P begins with the initial boundary assumption of one pressure release surface and five rigid walls. The mode functions Ψ_m are calculated with cosines, $\Psi(x, y, z) = A\cos(k_{m_x}x)\cos(k_{m_y}y)\cos(k_{m_z}z)$, and absorption is accounted for inside the final calculation of the Green's function:

$$g(\vec{r}) \approx \sum_{m=0}^{\infty} \frac{\Psi_m(\vec{r_0})\Psi_m(\vec{r})}{V\Lambda_m\left\{k^2 - k_m^2 - jk\left[\frac{<\alpha>_S S}{4V}\right]\right\}}, \tag{2}$$

where V is the volume of the tank and $\Lambda_m = \Lambda_{m_x,m_y,m_z} = \frac{1}{\epsilon_{m_x}\epsilon_{m_y}\epsilon_{m_z}}$ with $\epsilon_{m_x,m_y} = \{1 \text{ for } m_{x,y} = 0; 2 \text{ for } m_{x,y} \neq 0\}$ and $\epsilon_{m_z} = 2$. Equation (2) includes the total boundary surface area S, the acoustic wavenumber $k = w/c_{\text{liquid}}$ and the total modal wavenumber $k_m = \sqrt{k_{m_x}^2 + k_{m_y}^2 + k_{m_z}^2}$. The modal wavenumber components are $k_{m_x} = \frac{m_x\pi}{L_x}$, $k_{m_y} = \frac{m_y\pi}{L_y}$, and $k_{m_z} = \frac{(2m_z-1)\pi}{2L_z}$. The tank dimensions are defined as L_u, where u represents an x, y, or z, and the corresponding mode numbers are $m_u = (1, 2, 3, ...)$. An effective and spatially averaged absorption term $< \alpha >_S$ can be found from the Norris-Eyring equation,[14] though the current work uses an approximation based on impedances:

$$\begin{aligned} < \alpha >_S &= \alpha_{\text{air}}\frac{S_{\text{air}}}{S_{\text{total}}} + \alpha_{\text{wall}}\frac{S_{\text{wall}}}{S_{\text{total}}} \\ \alpha_{\text{wall}} &= 1 - \frac{Z_{\text{water}} - Z_{\text{wall}}}{Z_{\text{water}} + Z_{\text{wall}}} \\ \alpha_{\text{air}} &= 1 - \frac{Z_{\text{water}} - Z_{\text{air}}}{Z_{\text{water}} + Z_{\text{air}}}, \end{aligned} \tag{3}$$

with the impedance values of water Z_{water}, wall material Z_{wall}, and air Z_{air} obtained from average standard values. These values are listed in Table 1. The absorption calculation in Eq. (3) uses the surface area of the water-air surface S_{air}, the wall surface area S_{wall}, and a total surface area S_{total}. The pressure field $\hat{p}$ is calculated as $\hat{p}(\vec{r}) = \hat{A}g(\vec{r})$, where $\hat{A}$ is the freqency-dependent source amplitude. The modeled pressure field is compared to measurements in Sec. 4.

Table 1: Impedance Z and speed of sound c values used in Eq.* (3) *to estimate the spatially averaged absorption. Water and air properties match the code on Novak's website.[15] Acrylic properties found in Ref. 16.

Material	Z(kg/m^2/s)	c(m/s)
Liquid (Water)	1.5 e6	1488
Air	416	340
Wall (Acrylic)	3.26 e6	2750

B. MODEL N

In a paper by Novak *et al.*,[2] measured data from 1 kHz - 8 kHz is compared to an idealized model with all pressure release sides and their proposed model that incorporates an empirical wall damping term. When comparing these two models to data, the proposed model has a nearly perfect agreement with the data in Fig. 1 of Ref. 2 when using 15 modes. This proposed model begins by assuming all pressure release boundaries and then follows the equations provided below to account for finite impedance walls. The code to calculate this model is available online on Novak's website.[15]

A central feature of the proposed model is a method to improve the estimates of the wavenumber, k_m, to account for wall losses. The proposed model begins by calculating an initial wavenumber k_m:

$$k_m = \sqrt{k_{m_x}^2 + k_{m_y}^2 + k_{m_z}^2}, \tag{4}$$

where $k_{m_u} = \frac{m_u \pi}{L_u}$. The u represents an x, y or z, L_u is a tank dimension, and the mode number $m_u = (0, 1, 2, 3, ...)$. The k_m defined in Eq. (4) are used to estimate the zeroth order modulus of the modal wavenumbers for the tank wall $k_m^{(\text{wall})}$ and air $k_m^{(\text{air})}$:

$$\begin{aligned} k_m^{(\text{wall})} &= \frac{c_{\text{liquid}}}{c_{\text{wall}}} k_m \left(1 - i\delta_w\right) \\ k_m^{(\text{air})} &= \frac{c_{\text{liquid}}}{c_{\text{wall}}} k_m, \end{aligned} \tag{5}$$

that account for minor additional absorption. The water losses are assumed to be negligible, while the wall losses are accounted for with an empirical wall damping value $\delta_w = 0.022$. The sound speeds in Eq. (5) are the speed of sound in water, c_{liquid}, the speed of sound in the tank walls, c_{wall}, and the speed of sound in air, c_{air} (See Table 1). Then the modal wavenumber component for walls in the u direction are estimated as

$$k_{m_u}^{(\text{wall})} = -i\sqrt{-\left(k_m^{(\text{wall})}\right)^2 + \left(k_{m_{u'}}\right)^2 \left(k_{m_{u''}}\right)^2}. \tag{6}$$

In the above equation, u' and u'' indicate the directions x, y, z that are not u. For example, if $u = y$ then $u' = x$ and $u'' = z$. A similar expression is used for wavenumber components $k_{m_u}^{(\text{air})}$, $k_{m_u}^{(\text{wall})}$, and $k_{m_u}^{(\text{liquid})}$. These wavenumber components are used to calculate the impedance $\zeta_{u_j m}$ for every boundary:

$$\zeta_{u_j m} = \frac{\xi_{m_u}^{(\text{air,liquid})} + i\xi_{m_u}^{(\text{wall,liquid})} \tan\left(k_{m_u}^{(\text{wall})} h\right)}{1 + \xi_{m_u}^{(\text{air,wall})} \tan\left(k_{m_u}^{(\text{wall})} h\right)}, \tag{7}$$

where $\xi_{m_u}^{(\alpha,\beta)} = \frac{z_\alpha}{z_\beta} \frac{k_{m_u}^{(\beta)}}{k_m^{(\beta)}} \frac{k_m^{(\alpha)}}{k_{m_u}^{(\alpha)}}$ and h represents the thickness of the tank walls. Becasue each direction u has two boundaries, the six boundary impedances are denoted $\zeta_{u_j m}$, $j = 1, 2$. Then the wavenumbers k_{m_u} are recalculated with

$$k_{m_u} L_u \cong m_u \pi + i\left(\zeta_{u_1 m} + \zeta_{u_2 m}\right) \tag{8}$$

to include the impedances from Eq. (7). The complex expressions for the eigenfunctions Ψ_m combine the new wavenumbers with impedances using sine functions:

$$\Psi_m(x, y, z) = A \sin\left(k_{m_x} x - i\zeta_{x_1 m}\right) \sin\left(k_{m_y} y - i\zeta_{y_1 m}\right) \sin\left(k_{m_z} z - i\zeta_{z_1 m}\right), \tag{9}$$

where $A = \sqrt{2^3 / \left(L_x L_y L_z\right)}$. Then the Green's function is calculated with

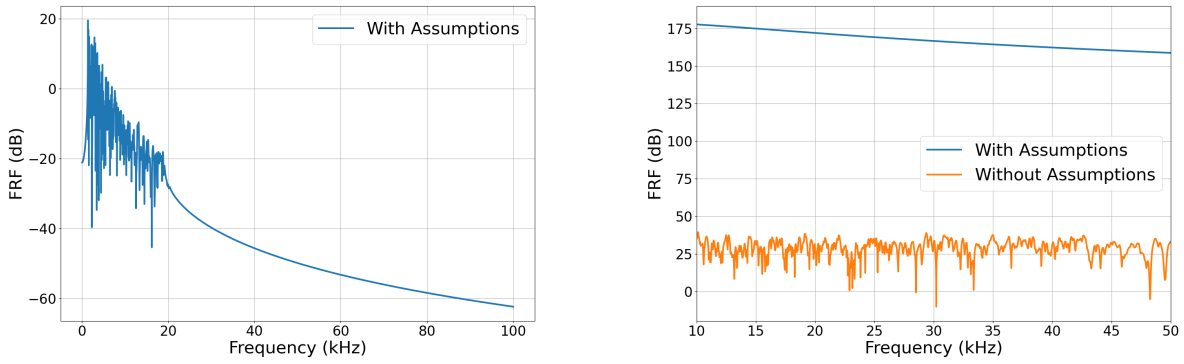

(a) *(b)*

Figure 5: (a) Original Model N for a glass tank with our tank geometry (b) Model N for our acrylic tank with original assumptions (blue line) and with assumptions removed (orange line).

$$P(x,y,z) = \sum_{m=0}^{\infty} \frac{\Psi_m(x_0,y_0,z_0)}{k_m^2 - k^2} \Psi_m(x,y,z). \tag{10}$$

This frequency dependent Green's function (using 15 modes) shows remarkable agreement with the data from small tanks (See Fig. 1 in Ref. 2).

i. Differences

Because of difference in size and frequency band of interest, Model N needs to be adjusted for our laboratory tank. The Green's function across frequency (a.k.a the frequency response function, FRF) for the original Model N for our tank geometry, but assuming glass walls instead of acrylic is shown in Fig. 5(a). The source position is $(0.41, 2.13, 0.25)$ and the receiver position is $(0.41, 1.83, 0.25)$ for the data in Fig. 5. The uncharacteristic decay that begins at 20 kHz is because the original Model N uses only 15 modes in calculation. Our tank model requires a higher number of modes as we are interested in a larger and higher frequency band than the 1 kHz - 8 kHz in the paper by Novak *et al.*[2] Instead of using 15 modes, we used $m_x = m_z = 120$ and $m_y = 200$. These mode numbers were found by steadily increasing the mode numbers in the x, y, and z directions until the shape of the FRF between 10 Hz - 100 kHz remained the same. When the original Model N is used with all the parameters of our tank including acrylic walls, the FRF is the blue line in Fig. 5(b), which shows almost no variation across frequency.

The assumptions included with the original Model N calculation are not applicable for our experimental setup due to the difference in tank wall material and tank size. The tanks used in experiments by Novak *et al.*[2] were made of thin glass while our tank is thick acrylic. The properties of acrylic produce an impedance much closer to the impedance of water than the impedance of glass or air. The thickness of our acrylic tank is 2.54 cm while the tanks used in Ref. 2 were 2.7 mm. In addition to differing wall parameters, both experiments had dramatically different tank sizes. Our laboratory tank is 3.66 m long by 1.22 m wide with a maximum water depth of 0.91 m. In Ref. 2 the largest tank is 58.6 cm long by 28.9 cm wide and 18.4 cm deep and the smallest tank is 39.4 cm long by 19.3 cm wide and 13.7 cm deep.

ii. Model N Without Assumptions

These differences in tank wall thickness, material, and size make it necessary to adjust the assumptions made in the original Model N calculation. For our Model N, we begin at the same point as the original. Instead of using 15 modes like the original Model N calculation, we used $m_x = m_z = 120$ and $m_y = 200$. Increasing the number of modes used increases the frequency range of Model N, allowing us to observe the full range of frequencies most commonly used in our tank measurements. We also adjusted the initial boundary conditions to assume more realistic boundaries — one pressure release surface and five finite impedance walls. First k_{m_z} in Eq. (4) is changed to be $k_{m_z} = \frac{(2m_z-1)\pi}{2L_z}$ to account for the pressure release z boundary at the water-air surface. In Eq. (5), a δ_w value of 0.3 was found for our tank by a grid search. These adjustments are used in Eqs. (4) - (7). As the approximation in Eq. (8) is based on the assumption that the impedance is a small factor, k_{m_u} is calculated instead with

$$k_{m_u} L_u = m_u \pi - \frac{i}{2} \ln \left(R_{u_1 m} R_{u_2 m} \right), \tag{11}$$

where $R_{u_j m} = -\frac{1-\zeta_{u_j m}}{1+\zeta_{u_j m}}$. In this equation, $j = 1, 2$ indicate the two boundaries in the u direction. A new complex expression for Ψ_m combines the new wavenumbers in Eq. (11) with finite impedance walls using $B_{m_u} = \frac{1}{R_{u_1 m}}$:

$$\Psi_m(x, y, z) = A_m \left(e^{-ik_{m_x} x} + B_{m_x} e^{ik_{m_x} x} \right) \left(e^{-ik_{m_y} y} + B_{m_y} e^{ik_{m_y} y} \right) \left(e^{-ik_{m_z} z} + B_{m_z} e^{ik_{m_z} z} \right). \tag{12}$$

The Green's function in Eq. (10) is then used to calculate the pressure field P. After removing these several assumptions, Model N returns the orange line in Fig. 5(b), which is dramatically different than with the assumptions.

4. RESULTS

The first data-model comparison is for a swept sine signal of 10 kHz to 50 kHz with a sampling frequency of 500 kHz and a water depth $h_w = 0.47$ m. Both source and receiver hydrophones were positioned in the middle of the x axis and at half the water depth: $x = 0.6$ m and $z = 0.235$ m. Measurements were made with the projecting and receiving transducers 0.3, 0.6, and 1.0 m apart in the y direction. A schematic of the experiment setup depicted in Fig. 6 shows a red dot at the source position and purple dots at the receiver positions. In Fig. 7, three plots are shown depicting the modeled and measured FRFs for the three distances. Model N is in blue, Model P in black, and the data in red. To compare the models to the data, we examine the moving average in each case and look for frequencies or ranges where the moving average appears to stay level, increase, or decrease. In each range case, both models have a relatively flat average over the frequency range 10 kHz - 50 kHz. Whereas, in each case the measured data starts flat at 10 kHz, increases from 25 kHz - 35 kHz, and then decreases while approaching 50 kHz.

The second experiment used sine waves at different frequencies measured at source-receiver ranges from 0.1 - 1.6 m. The experiment was set up similarly to the frequency range data described above, but with 150

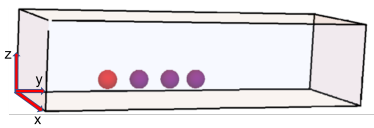

Figure 6: Experiment schematic with the red dot as the source position and purple dots as receiver positions

receiver positions between 0.1 - 1.6 m. Each sine wave signal sent in the tank was 2 seconds long with a sampling frequency of 500 kHz. Each measurement was completed with both h_w = 0.47 m and h_w = 0.24 m. In each of the plots in Fig. 8 and Fig. 9, the models and data are presented as relative transmission loss to remove the impact of source level. Figure 8 shows results with h_w = 0.47 m and Fig. 9 with h_w = 0.24 m. Experiments with the source and receiver at the same depth are plotted as (a), (b), (c) in each figure. While the experiments with the source at two thirds h_w (measured from the bottom of the tank) and the receiver at one third h_w are (d), (e), (f) in both Fig. 8 and Fig. 9. These plots show the source signal at 10 kHz, 32 kHz, and 53 kHz as examples.

The measured data at each frequency are plotted as functions of range in Fig. 8 and 9 (orange lines). The values are received levels relative to the level at 0.1 m; relative levels are chosen to remove the impact of the source level. The use of relative transmission loss reduces the relative uncertainty in horizontal range to that of the precision of a single UR10e robotic arm of 0.01 mm.[6] Thus, the uncertainty in the spacing between the measurements is approximately 0.01 mm. The other source of positioning error is the distance between the UR10e robotic arm holding the projecting transducer and the one holding the receiving transducer. The distance between the center of the bases of the robotic arms was measured with a tape measure and has an estimated uncertainty of 0.25 cm. The positioning uncertainty can shift the data (orange line) slightly left or right but also up and down because the plotted level are relative to the range labeled 0.1 m. Despite the positioning uncertainty and removed assumptions, Model N and Model P in Fig. 8 and 9 do not provide an excellent data-model comparison as found in Fig. 1 of Ref. 2. Future work is required to determine why these Cartesian models do not represent sound propagation in large tanks.

5. CONCLUSION

The water tank in BYU's underwater acoustics laboratory is being characterized and various sound propagation models are being explored. Two Cartesian normal-mode models that begin with different ideal boundary conditions and incorporate finite impedance were compared to data. Model P is commonly used in room acoustic and assumes five finite impedance walls with one pressure release surface. Model N begins with all pressure release surfaces and incorporates wall losses. The original Model N showed excellent agreement for small glass tanks, which made us curious if it could be adapted for our larger tank. Adjustments were made to the original Model N to remove assumptions that did not coincide with the parameters of our laboratory tank. Both Model N and Model P were then compared to data in experiments over frequency range and distance. Data-model comparisons may have areas of interest dependent on frequency and the distance of the hydrophones, but overall these two models do not match the modal interference pattern exhibited in the data. Future work is needed to explore other models, such as a ray tracing model. A good model for sound propagation in the tank will allow us to simulate the sound field for optimization problems, create accurate training data for machine learning applications, and test generalizability to the measured data.

REFERENCES

[1] A. D. Pierce, *Acoustics: An Introduction to Its Physical Principles and Applications*, 3rd ed. (Springer, 2019), pp. 328–335.

[2] A. Novak, M. Bruneau, and P. Lotton, "Small-sized rectangular liquid-filled acoustical tank excitation: A modal approach including leakage through the walls," Acta Acustica united with Acustica **104**(4), 586–596 (2018) 10.3813/AAA.919199.

[3] J. D. Sagers, "Results from a scale model acoustic propagation experiment over a translationally invariant wedge," in *Proceedings of Meetings on Acoustics 168ASA*, Acoustical Society of America (2014), Vol. 22, p. 070001.

[4] J. D. Sagers and M. S. Ballard, "Testing and verification of a scale-model acoustic propagation system," The Journal of the Acoustical Society of America **138**(6), 3576–3585 (2015).

[5] Y.-M. Zhang, R. Tang, Q. Li, and D.-J. Shang, "The low-frequency sound power measuring technique for an underwater source in a non-anechoic tank," Measurement Science and Technology **29**(3), 035101 (2018).

[6] C. T. Vongsawad, T. B. Neilsen, A. D. Kingsley, J. E. Ellsworth, B. E. Anderson, K. N. Terry, C. E. Dobbs, S. P. Hollingsworth, and G. H. Fronk, "Design of an underwater acoustics lab," Proc. Mtgs. Acoust **45**, 70005 (2021) https://doi.org/10.1121/2.0001540 10.1121/2.0001540.

[7] G. D. Curtis, "Wide-frequency response of type J-9 underwater sound projector in a typical experimental tank," The Journal of the Acoustical Society of America **826** (1979) 10.1121/1.382504.

[8] A. J. Berkhout, D. de Vries, and M. M. Boone, "A new method to acquire impulse responses in concert," The Journal of the Acoustical Society of America **179** (1980) 10.1121/1.384618.

[9] A. Farina, "Advancements in impulse response measurements by sine sweeps," October, Audio Engineering Society (2007).

[10] B. Van Damme, K. Van Den Abeele, Y. Li, and O. Bou Matar, "Time reversed acoustics techniques for elastic imaging in reverberant and nonreverberant media : An experimental study of the chaotic cavity transducer concept," Journal of Applied Physics **95** (2011) 10.1063/1.3590163.

[11] J. L. Kennedy, T. M. Marston, K. Lee, J. L. Lopes, and R. Lim, "A rail system for circular synthetic aperture sonar imaging and acoustic target strength measurements : Design / operation / preliminary results," Review of Scientific Instruments **014901** (2014) 10.1063/1.4861353.

[12] B. E. Anderson, M. Clemens, and M. L. Willardson, "The effect of transducer directivity on time reversal focusing," The Journal of the Acoustical Society of America **142**(1), EL95–EL101 (2017) http://dx.doi.org/10.1121/1.4994688 10.1121/1.4994688.

[13] K. L. Gemba and E.-m. Nosal, "Source characterization using recordings made in a reverberant underwater channel," Applied Acoustics **105** (2016) http://dx.doi.org/10.1016/j.apacoust.2015.11.008 10.1016/j.apacoust.2015.11.008.

[14] G. C. Eastland and W. C. Buck, "Reverberation characterization inside an anechoic test chamber at the Weapon Sonar Test Facility at NUWC Division Keyport," **030003** (2017) 10.1121/2.0000508.

[15] A. Novak, "AAA: Acoustics of a Fish-Tank" , Code available online (2018), https://ant-novak.com/posts/research/2018-07-29_AAA_FishTank/.

[16] A. Selfridge, "Approximate material properties in isotropic materials," IEEE Transactions on Sonics and Ultrasonics **32**(3), 381–394 (1985) 10.1109/T-SU.1985.31608.

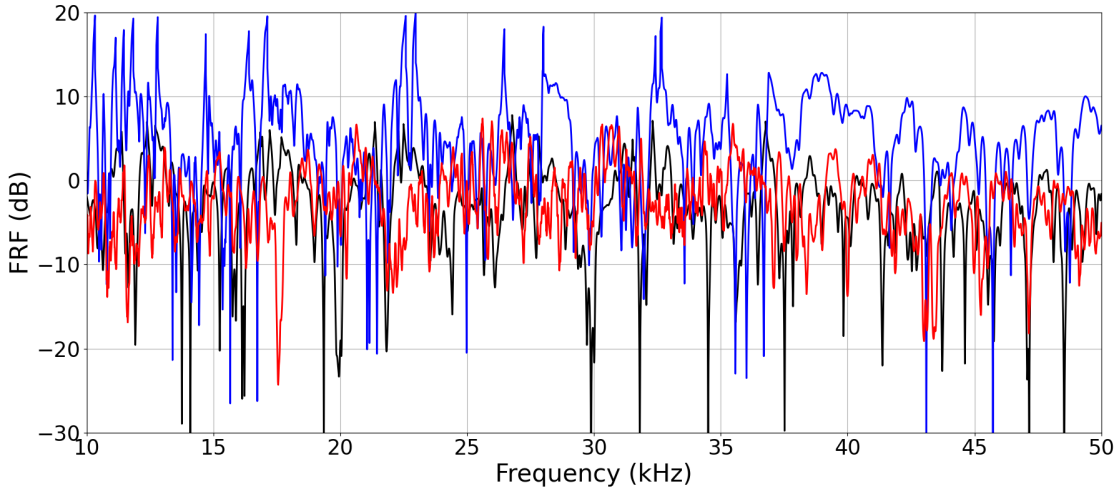

(a)

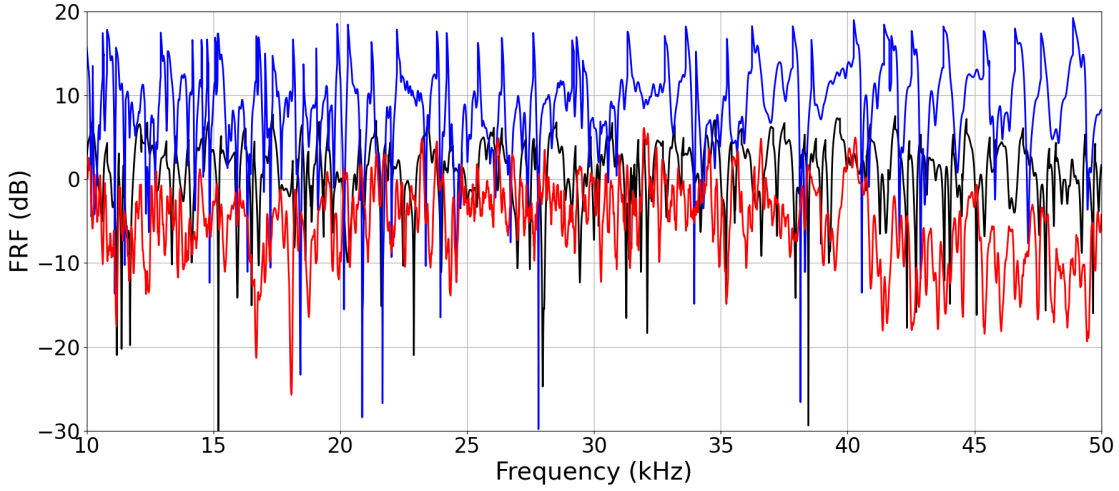

(b)

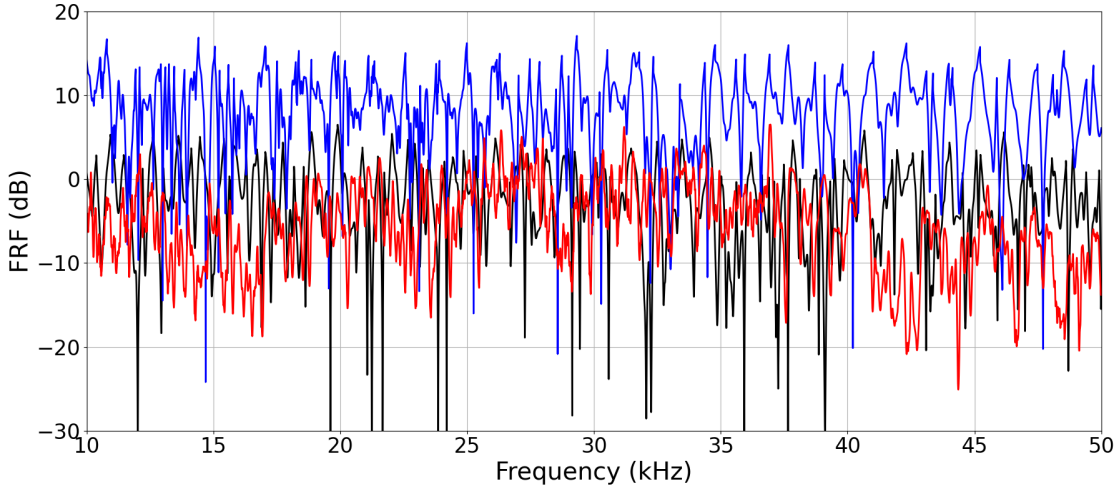

(c)

Figure 7: Model N is blue, Model P is black, and the data is red. (a) Range of 0.3 m (b) Range of 0.6 m (c) Range of 1 m

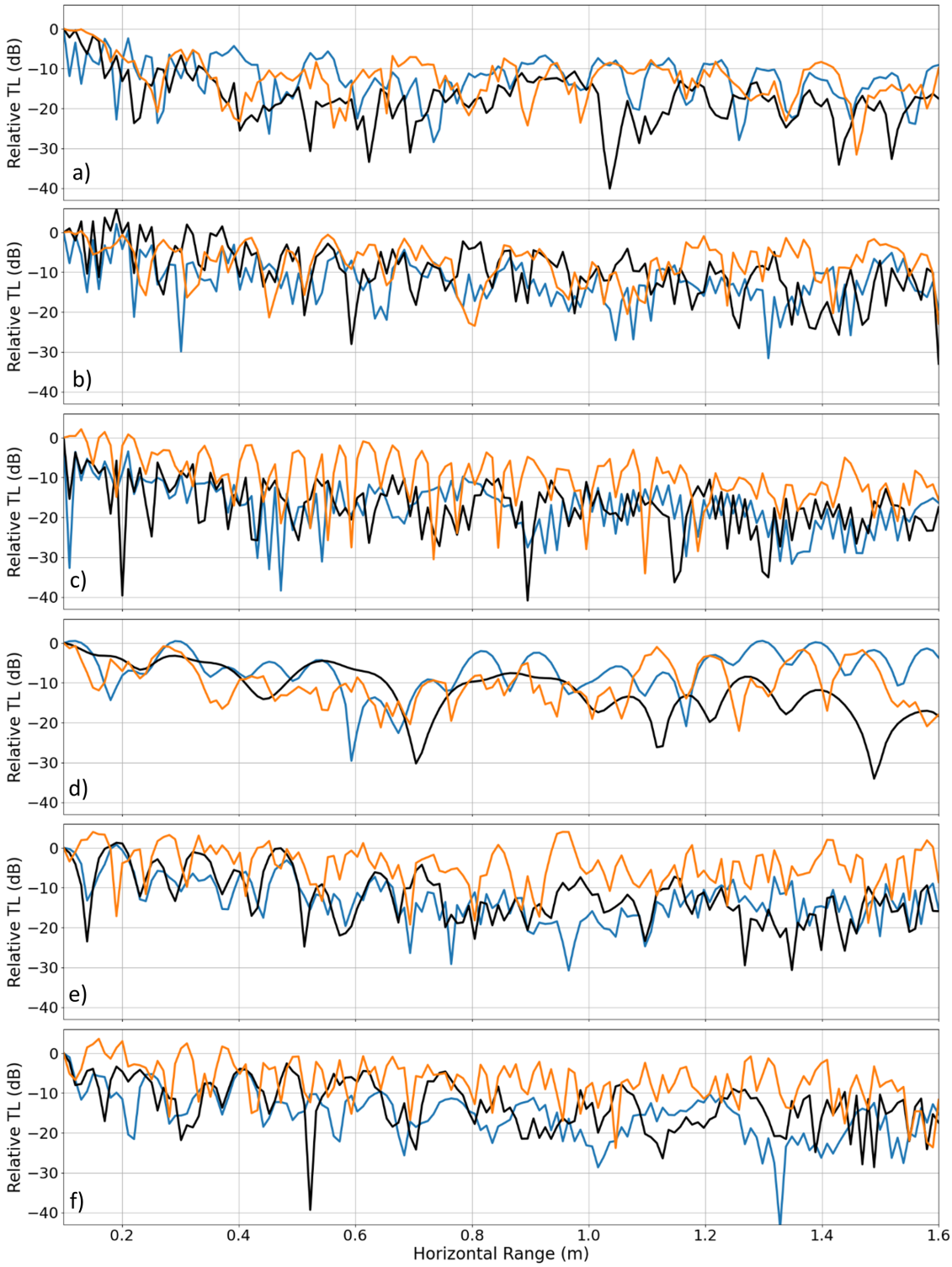

Figure 8: Levels from Model N (blue), Model P (black), and the data (orange) relative to the level at range = 0.1 m for h_w = 0.47 m. Figures (a) 10 kHz, (b) 32 kHz, and (c) 53 kHz have the source and receiver at the same z at $h_w/2$. Figures (d) 10 kHz, (e) 32 kHz, (f) 53 kHz have the source at $z = 2h_w/3$ and the receiver at $h_w/3$.

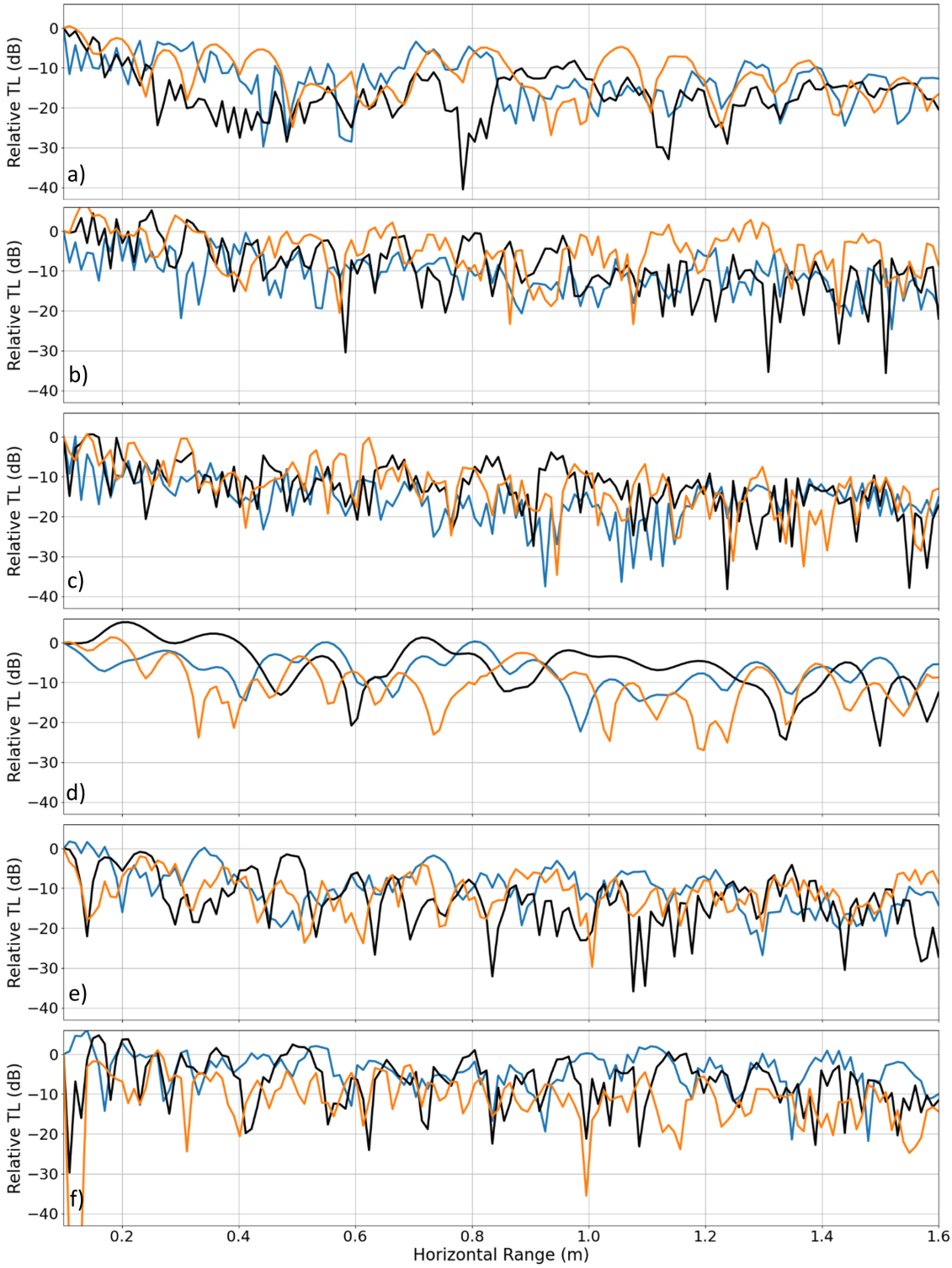

Figure 9: Comparing relative transmission loss of Model N (blue), Model P (black), and the data (orange) at h_w=0.24 m. Figures (a) 10 kHz, (b) 32 kHz, and (c) 53 kHz have the source and receiver at the same z at $h_w/2$. Figures (d) 10 kHz, (e) 32 kHz, (f) 53 kHz have the source at $z = 2h_w/3$ and the receiver at $h_w/3$.